MATERIALS SCIENCE

Full-color fiber light-emitting diodes based on perovskite quantum wires

Beitao Ren[1,2,3], Daquan Zhang[1,2,3], Xiao Qiu[1,2,3], Yucheng Ding[1,2,3], Qianpeng Zhang[1,2,3], Yu Fu[4], Jin-Feng Liao[5], Swapnadeep Poddar[1,2,3], Chak Lam Jonathan Chan[1,2,3], Bryan Cao[1,2,3], Chen Wang[1,2,3], Yu Zhou[1,2,3], Dai-Bin Kuang[5], Haibo Zeng[6], Zhiyong Fan[1,2,7,3]*

Fiber light-emitting diodes (Fi-LEDs), which can be used for wearable lighting and display devices, are one of the key components for fiber/textile electronics. However, there exist a number of impediments to overcome on device fabrication with fiber-like substrates, as well as on device encapsulations. Here, we uniformly grew all-inorganic perovskite quantum wire arrays by filling high-density alumina nanopores on the surface of Al fibers with a dip-coating process. With a two-step evaporation method to coat a surrounding transporting layer and semitransparent electrode, we successfully fabricated full-color Fi-LEDs with emission peaks at 625 nanometers (red), 512 nanometers (green), and 490 nanometers (sky-blue), respectively. Intriguingly, additional polydimethylsiloxane packaging helps instill the mechanical bendability, stretchability, and waterproof feature of Fi-LEDs. The plasticity of Al fiber also allows the one-dimensional architecture Fi-LED to be shaped and constructed for two-dimensional or even three-dimensional architectures, opening up a new vista for advanced lighting with unconventional formfactors.

INTRODUCTION

Flexible optoelectronic devices, light-emitting diodes (LEDs) in particular, have been playing an important role in multifarious applications, including wearable displays, health monitoring systems, virtual reality, optical communications, automotive lighting, etc. (*1*–*6*) Now, various types of advanced technologies, such as emitter-coated fibers, nanostructural materials, and polymer- and elastomer-based substrates, have been developed for high-performance flexible LEDs (*1*, *7*–*10*). Among them, fiber LED (Fi-LED), which emits light from a flexible substrate that resembles a fiber, exhibits marked advantages over the others in wearable displays due to its good compatibility with textiles fabrication, as well as excellent spatial luminance uniformity.

Metal halide perovskites (MHPs) have carved a niche for themselves as one of the most promising light-emitting materials for next-generation LEDs, owing to their intrinsically marvelous optoelectronic features, including effective radiative carrier recombination, remarkable color tunability and purity, as well as facile synthesis and low-temperature fabrication processes in both liquid and vapor phases (*11*–*14*). Attributed to the well-developed approaches for interface engineering and structure optimization for perovskite LED (PeLED) devices, the external quantum efficiency (EQE) of PeLED has been boosted from less than 1% to nearly 30%, within a decade (*15*–*17*). Meanwhile, MHPs were also successfully incorporated into upcoming technologies, such as large-scale, flexible, and multifunctional LEDs (*18*–*21*), suggesting their great potential in wearable displays. However, MHP-based Fi-LEDs have remained underexplored because of challenges in fabrication, such as gravity and surface tension–induced nonuniform coating, low-quality crystallization, complex process for electrode deposition, etc., which culminate in uneven and inefficient light emission.

Here, we demonstrate full-color Fi-LEDs based on MHP quantum wires (PeQWs) with good bendability, stretchability, and moisture stability. Serving as a growth template, porous alumina membrane (PAM) with an ultrasmall pore size of ~5 nm is fabricated on thin aluminium (Al) fibers for growing all-inorganic PeQWs by a roll-to-roll solution-coating process. With the combination of quantum confinement effect and the passivation from the three-dimensional (3D) PAM structure, the as-grown PeQWs demonstrate prominent photoluminescence quantum yield (PLQY) of nearly 90% and a noticeable photoluminescence (PL) lifetime (T_{PL50}) of up to 1500 hours under ambient condition. The obtained Fi-LEDs behave graceful full-color fabric electroluminescence (EL), and the corresponding planar PeLED devices with the optimal structure achieved a relatively high EQE of 15.2%, when compared to all-inorganic PeLEDs (*22*). With extra polydimethylsiloxane (PDMS) encapsulation, a variety of EL scenarios are demonstrated with the full-color Fi-LED devices, highlighting great potentials of MHP Fi-LEDs in flexible and wearable lighting and displays.

RESULTS

The schematic illustration depicting the growth of PeQWs is shown in Fig. 1A. A solution dip-coating method was adopted with a fiber-compatible roll-to-roll system. MHP precursor [$CsPbX_3$ (X = Cl, Br, I, or mixed halide)] solution is filled into PAM channels which are fabricated on a thin (0.1, 0.3, or 0.5 mm in diameter) Al fiber with a 5-V anodic anodization process. A surrounding annealing procedure with a heating coil is subsequently carried out for spatially uniform solvent vaporization and MHP crystallization. It is noted that

[1]Department of Electronic and Computer Engineering, The Hong Kong University of Science and Technology, Clear Water Bay, Kowloon, Hong Kong SAR, China. [2]State Key Laboratory of Advanced Displays and Optoelectronics Technologies, HKUST, Clear Water Bay, Kowloon, Hong Kong SAR, China. [3]Guangdong-Hong Kong-Macao Joint Laboratory for Intelligent Micro-Nano Optoelectronic Technology, HKUST, Clear Water Bay, Kowloon, Hong Kong SAR, China. [4]School of Advanced Energy, Shenzhen Campus of Sun Yat-sen University, Shenzhen 518107, P. R. China. [5]MOE Key Laboratory of Bioinorganic and Synthetic Chemistry, Lehn Institute of Functional Materials, School of Chemistry, Sun Yat-sen University, Guangzhou 510275, P. R. China. [6]MIIT Key Laboratory of Advanced Display Materials and Devices, Institute of Optoelectronics and Nanomaterials, School of Materials Science and Engineering, Nanjing University of Science and Technology, Nanjing 210094, P. R. China. [7]Department of Chemical and Biological Engineering, The Hong Kong University of Science and Technology, Clear Water Bay, Kowloon, Hong Kong SAR, China.
*Corresponding author. Email: eezfan@ust.hk

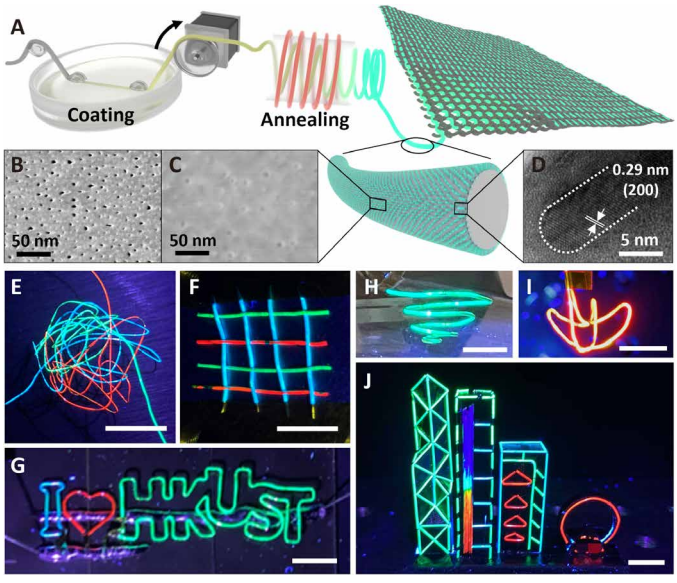

Fig. 1. PeQWs Fabrication. (**A** to **D**) Schematic of PeQWs growth with PAM template (A) and the corresponding top view SEM images of PAM on Al fiber before (B) and after (C) $CsPbBr_3$ QWs formation, as well as the HRTEM image (D) of a single $CsPbBr_3$ QW extracted from PAM template. (**E** to **J**) Fluorescent pictures: colorful tangled fibers (E), woven fibers (F), I Love HKUST pattern (G), green swirl (H), HKUST Redbird logo (I), and Victoria Harbor (J) built by mounting batches of fibers. All the unlabeled scale bars are 1 cm.

the Wenzel state enables rough PAM surface more hydrophilic and then better wettability than its original status on smooth Al surface (*23*), which is proved by a decreased contact angle of MHP precursor [in dimethyl sulfoxide (DMSO)] (fig. S1). During soaking our PAM@Al fiber in MHP precursor, Wenzel state allows the solution to completely infiltrate into PAM channels such that the PeQW array can be uniformly grown. To minimize the formation of MHP thin-film (TF) structure on the PAM surface, the residual solution is removed by nitrogen (N_2) blowing before annealing for solvent vaporization and MHP crystallization. As a result, a nearly 100% filling ratio and clean surface can be observed by comparing the top-view scanning electron microscopy (SEM) images of PAM before (Fig. 1B) and after (Fig. 1C) $CsPbBr_3$ QWs growth. The corresponding cross-sectional SEM images in fig. S2 and top-view morphology comparison between QWs and TF structure in fig. S3 also provide the evidence for the absence of extra TF structure on the surface postcoating. In addition, because of quantum confinement effect and the exclusion of surface tension during dip-coating, $CsPbBr_3$ QWs provide more uniform and brighter luminescence under ultraviolet (UV) stimulus than $CsPbBr_3$ TF (insets in fig. S3). The obtained well-crystallized single $CsPbBr_3$ QW extracted from the PAM channel can be characterized by high-resolution transmission electron microscopy (HRTEM) technology, as shown in Fig. 1D, where an interplane spacing of 0.29 nm can be seen and assigned to the distance between two neighbouring (200) planes. In fig. S4, a relatively intact and well-crystalized single PeQW with the length of ~50 nm is captured by scanning transmission electron microscopy (STEM) in lower magnification. The energy dispersive spectroscopy (EDS) mapping with caesium (Cs) and lead (Pb) elements (fig. S5) is also characterized by STEM to demonstrate the PeQW array.

The obtained PeQWs exhibit a typical fluorescent feature, and the emissive color is adjusted with the perovskite material compositions listed in table S1. Benefiting from the flexibility of thin Al fiber, the as-fabricated fibers can be easily tangled (Fig. 1E) and woven (Fig. 1F) to each other, revealing the potential in textile lighting application (Fig. 1A). Meanwhile, thin Al fiber has both malleability and plasticity, which allows it to be fashioned into diverse 2D and 3D architectures. Here, we showcase a 2D full-color string "I Love HKUST" (Fig. 1G), a 3D green swirl (Fig. 1H), and an HKUST Redbird pattern (Fig. 1I) with excellent fluorescence uniformity. In Fig. 1J, we combine various kinds of PeQWs to build up a "night scene" of Victoria Harbour, with the iconic buildings in Hong Kong, where a halide exchange method is used to acquire halide gradient for obtaining color transition regions (*24*, *25*). The low activation energies for defect or ion migration within the nanostructure, coupled with the high dynamic nature of the surface ions, allow the occurrence of halide exchange in PeQWs (*26*). Specifically, green $CsPbBr_3$ QWs undergo a halide exchange process with CsI and CsCl solutions to obtain $CsPbBr_xI_{3-x}$ and $CsPbBr_xCl_{3-x}$ gradient. It is reported that the MHP synthesized by ion exchange typically presents better phase stability than directly synthesized MHP (*27*). In fig. S6, the PL spectra of green–to–sky-blue (G-B) and green-to-red (G-R) transition regions are indicated with dual peaks or a plateau shape, thus realizing the multicolor fibers on the second building from the left. Our strategy with PeQWs growth on PAM@Al fiber opens up an innovative way for fabricating unconventional 3D-structured lighting sources.

To further study the crystallinity of our PeQWs, x-ray diffraction (XRD) patterns for three representative red/green/sky-blue (R/G/B) PeQWs are measured and shown in fig. S7. Distinctive peaks at 15.1°, 21.7°, and 30.7° are respectively classified to (110), (112), and (220) planes of orthorhombic $CsPbBr_3$ phase. The intensity differences and slight shift of specific peaks in the R- and B-PeQWs patterns can be attributed to the lattice expansion or contraction induced by lager I^- ion and smaller Cl^- ion (*28*). Figure 2A shows the absorption and PL spectra with the corresponding PL image of R/G/B PeQWs. In contrast to the traditional TF counterparts (PL spectra in fig. S8), PeQWs exhibit blue-shifted PL peaks due to the quantum confinement effect (*29*, *30*). The PL peaks of PeQWs are located at 625, 512, and 490 nm, respectively, with narrow full width at half maximum (FWHM) of 39, 18, and 20 nm. Meanwhile, the synergetic effect of the spatial confinement and surface passivation of the PAM template contribute to high PLQY values of 59.96, 87.11, and 65.10% for the R-, G-, and B-PeQWs, respectively (Fig. 2B), which are much higher than that of TF counterparts (*31*). To understand the mechanism for high PLQY in PeQWs, x-ray photoelectron spectroscopy (XPS) (fig. S9) and time-resolved photoluminescence (TRPL) measurement (fig. S10) are characterized. From XPS results, the dominant halide compositions in different PeQWs can be distinguished (fig. S9, A to C), and the slight right-shift to lower binding energy of Cs 3d, Pb 4f, and Br 3d spectra on $CsPbBr_3$ QW sample, respectively by 0.2, 0.2, and 0.4 eV (fig. S9, D to F), is also observed, suggesting the surface passivation effect from PAM template, thus suppressing nonradiative recombination on the PeQW surface (*32*). TRPL results show the average carrier lifetime (τ_{ave}) of 10.71, 6.40, and 5.57 ns, respectively, for R-, G-, and B-PeQWs. A short τ_{ave} can be typically caused by the increase of either or both radiative and nonradiative recombination (*19*, *33*). In our case, on the basis of the lower binding energy in XPS results and high PLQY, such a short

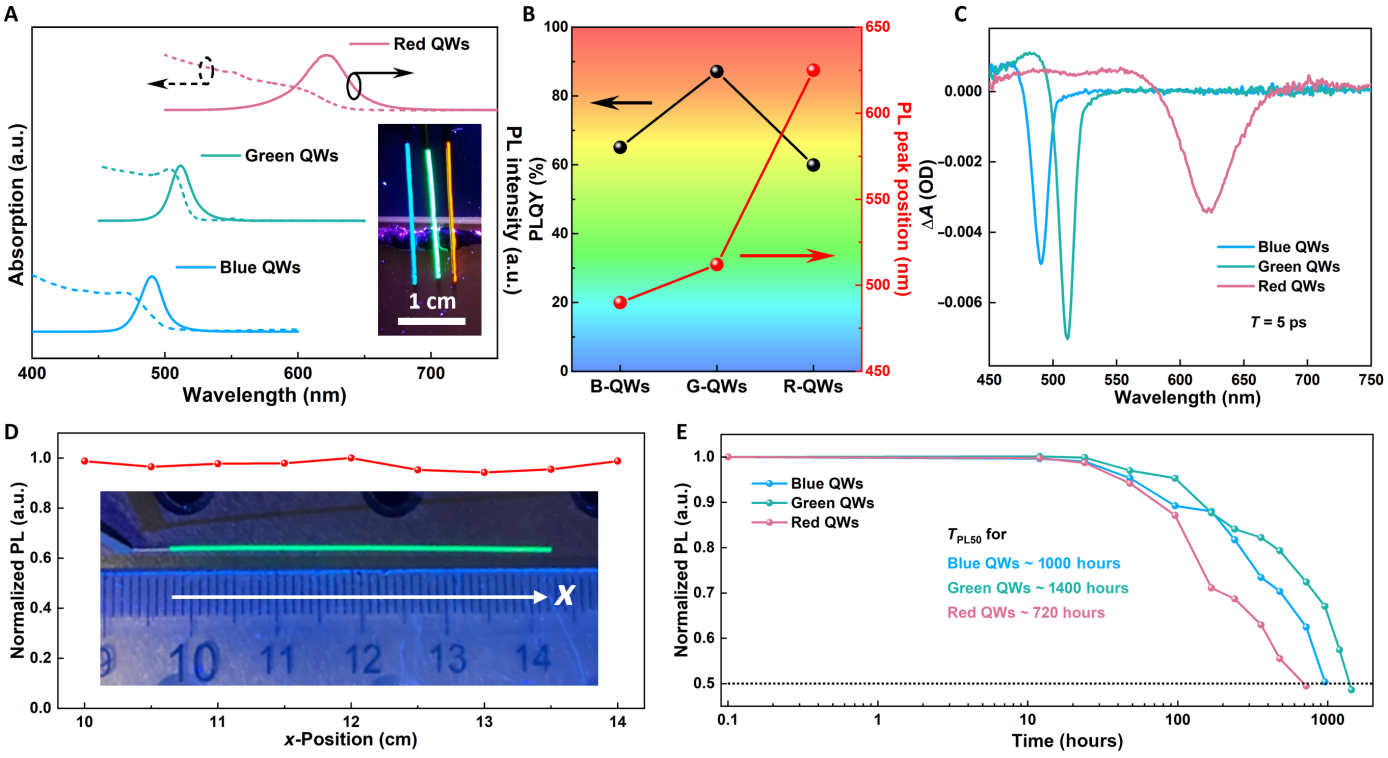

Fig. 2. PeQWs characterizations. (**A**) Absorption and PL spectra of three representative R/G/B PeQWs. The inset is the fluorescent image. (**B**) PLQY and PL peak position of PeQWs with different halide compositions. (**C**) TA spectra of PeQWs at the same delay time of 5 ps. (**D**) Normalized PL intensity evolution as a function of length position along a single fiber. The inset shows the fluorescent photograph of the corresponding green fiber. (**E**) PL stability test in ambient air (23°C, ~45 to 55% relative humidity). a.u., arbitrary units; OD, optical density.

τ_{ave} further validates the high radiative recombination rate in PeQWs. In addition, transient absorption (TA) measurement is conducted to study the energy transfer and recombination dynamics of photogenerated carriers in PeQWs. Figure 2C presents the single pronounced ground-state bleach (GSB) peaks for such PeQWs, at a delay time of 5 ps, which coincide with the PL peaks. As shown in fig. S11, a single narrow GSB peak for G-PeQWs indicates the absence of energy transfer and the coexistence of different phases, while for B- and R-PeQWs, a slight time-dependent red shift may be caused by halide segregation in mixed halide perovskite, which can be notably suppressed by using cationic additives (*17*, *34*). For our PeQWs, although devoid of any extra doping for defect passivation, the outstanding optical properties mentioned illustrate the superiority over conventional TF structure counterparts. Simultaneously, the highly uniform growth of PeQWs on the PAM@Al fiber is characterized by a position-dependent PL measurement with an over 4-cm-long sample along both the length (Fig. 2D, with the corresponding PL spectra in fig. S12) and radius directions (fig. S13). Furthermore, benefiting from the 3D protection of the PAM template from moisture and oxygen stimulus (*19*, *31*, *35*), the as-grown PeQWs exhibit an extraordinary PL lifetime in an ambient condition (23°C, 45 to 55% relative humidity), with the T_{PL50} values of ~720, ~1400, and ~1000 hours, respectively, for R-, G-, and B-PeQWs (Fig. 2E), where T_{PL50} is defined as the time when the PL drops to 50% of its initial intensity. The corresponding PL spectral evolutions of different PeQWs are denoted in fig. S14, which manifests relative spectral stability by spatially inhibiting the ambient air-induced ion migration, especially for the mixed halide B- and R-PeQWs. In addition to the Al foil, our PeQWs can also be easily grown on other types of substrates, such as widely used fluorine-doped tin oxide (FTO)–coated glasses and flexible stainless-steel foil. A thin layer of Al needs to be coated on the substrates either by sputtering or cold spray method (*19*, *36*), before the anodization process. The cross-sectional SEM images in fig. S15 (A and B), as well as the PL spectra in fig. S15C, indicate the successful growth of PeQWs on stainless-steel and FTO-coated glass, respectively. This feature enables PeQWs good compatibility in industry and high potential in practical applications.

To fabricate Fi-LED on the PeQW-based fiber, surrounding copper phthalocyanine (CuPc) and thin gold (Au) are conformably deposited with a two-step evaporation method (fig. S16), where CuPc serves as a hole transporting layer (HTL) and Au is a semi-transparent top electrode. Briefly, the as-prepared PeQW fiber is horizontally mounted on stage for evaporation on the front side and then is turned over 180° for the evaporation on the back side, so as to uniformly and continuously deposit surrounding CuPc and Au (fig. S17). Figure 3A presents the schematic of our Fi-LED device, where Al fiber is cathode terminal and surrounding Au is anode terminal when under forward bias. The insets in Fig. 3A show the cross-sectional schematic of device and its corresponding SEM image, indicating that an around 200-nm-thick PeQW array structure is used. The cross-sectional TEM image in fig. S18 can easily observe the vertically arranged PeQW array, with an ultrathin Al_2O_3 barrier layer (around 4 nm, indicated by red dashed lines) between PeQW array and Al substrate. An energy band structure for the fabricated

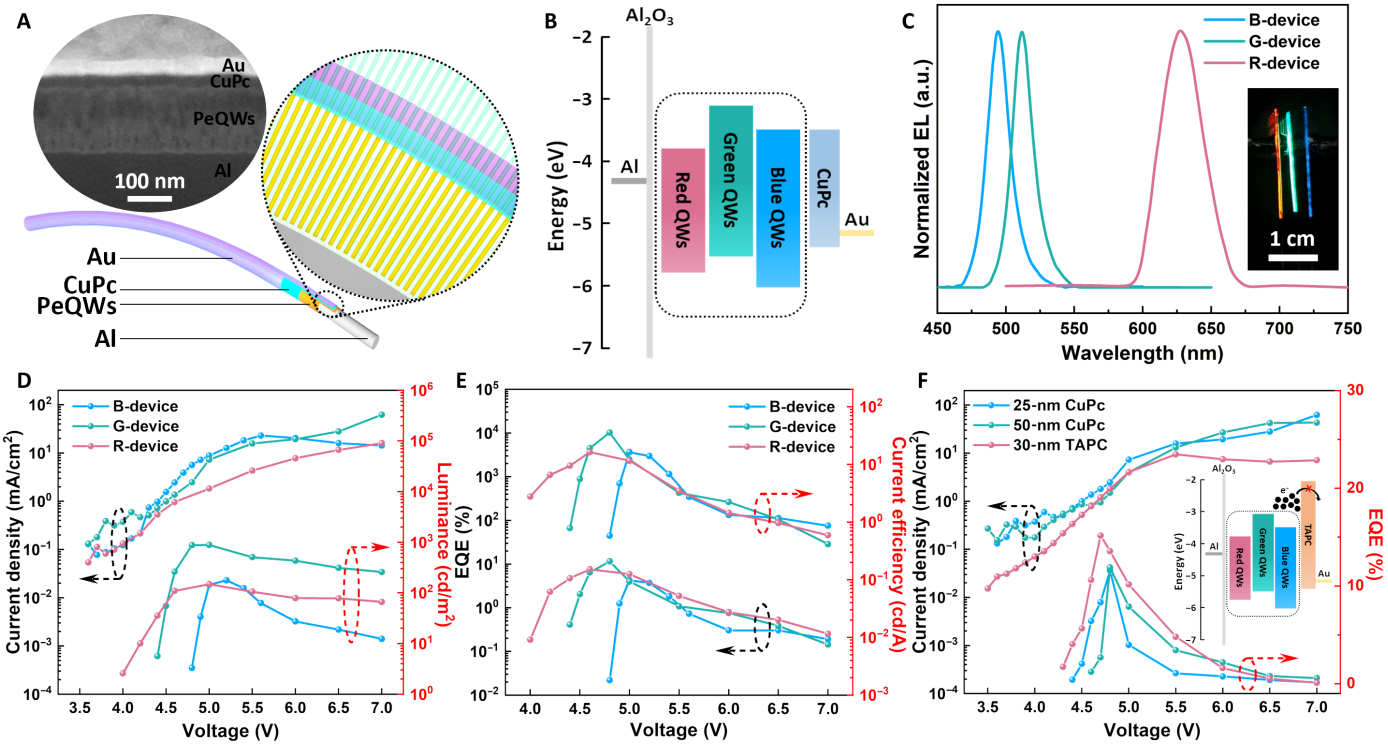

Fig. 3. PeQW-based Fi-LED structure and performance. (**A**) Device schematic. The inset at the top left corner shows the cross-sectional SEM image of device. (**B**) Energy band structure of the Fi-LED devices. (**C**) EL spectra of R/G/B LED devices. The inset is an EL photograph of Fi-LEDs with different colors. (**D** to **E**) Planar devices characterization: *J-L-V* (D) and EQE–current efficiency–voltage (E) curves of R/G/B LED devices. (**F**) Device characterizations with different HTLs. The inset indicates the modified energy band structure of TAPC devices for better electron blocking.

Fi-LED devices is plotted in Fig. 3B, where R/G/B devices are respectively with the R/G/B PeQWs active layer shown in dotted box. The valance band maximum values of those three PeQWs are determined with the UV photoelectron spectroscopy (UPS) results (fig. S19), and the bandgaps (E_g) are calculated with the corresponding PL peak positions because MHP is well-known as a direct bandgap material. Intriguingly, a metal-insulator-semiconductor (MIS) junction is formed in the Al/Al_2O_3/PeQWs structure, enabling an electron tunneling process through the ultrathin Al_2O_3 layer and its working mechanism has been clearly explained in other report (*37*), which can be proved by a linear dependence of I/V^2-$1/V$ plotting (fig. S20), where I is the integrated EL intensity and V is the bias voltage. When getting a high enough voltage bias for tunneling through the ultrathin Al_2O_3 layer, electrons undergo radiative recombination with holes in PeQW zone for light emission. Figure 3C shows the EL spectrum and the photograph of lighting Fi-LEDs under a constant 6-V forward bias, giving the EL peaks at 627, 512, and 494 nm for R-, G-, and B-devices, respectively, and narrow FWHM of 40, 20, and 18 nm. The corresponding Commission Internationale de l'éclairage chromaticity coordinate diagram is given in fig. S21, showing the emissive color coordinates of (0.65, 0.31), (0.07, 0.73), and (0.08, 0.32), respectively, positioned at red, green, and sky-blue regions. The consistent EL spectra under different bias voltages in fig. S22 demonstrate the good color stability of the mixed-halide Fi-LEDs, where slightly increased FWHM at higher bias voltage is believed to be caused by a field-induced quantum confinement Stark effect (*38*). EL variation is also quantified to be a value of 11.2% by studying the EL intensity distribution along both the length and radius directions (fig. S23). The length-dependent EL degradation is majorly resulted from the current spreading issue of the thin Au electrode, which typically can be addressed by depositing an extra layer of Au grid to improve the conductivity (*19*).

For a convenient experimental estimation of Fi-LED performance, planar devices with the exactly same device structure and similar fabrication procedures (Materials and Methods) are characterized. Figure 3D presents the current density-luminance-voltage (*J-L-V*) diagram of PeQW-based planar devices. Because of the existence of the barrier layer, the threshold of etch device is a little bit higher than that of traditional TF counterpart, showing 4.0, 4.4, and 4.8 V, respectively, for R-, G-, and B-PeQWs devices. In Fig. 3E, EQE–current efficiency–voltage diagram is calculated and plotted on the basis of *J-L-V* results, where EQE is determined by the ratio between the number of photons emitted and the number of electrons passing through the device. We can see that the champion EQE of 7.6, 11.6, and 4.3% are achieved for R-, G-, and B-PeQWs devices, respectively, at the luminance of 144, 876, and 110 cd m^{-2}. The lifetime measurement with an initial luminance (L_0) of 100 cd m^{-2} for all kinds of Fi-LEDs is carried out in ambient condition without encapsulation (fig. S24). The results present a moderate lifetime, and there is still a large room for improvement. Despite the relatively lower EQE and stability of our Fi-LEDs than that of the state-of-the-art planar PeLEDs, the exceptional quality of PeQWs underscores the potential for further optimization and the realization of highly efficient Fi-LEDs by tuning the PeQW composition

and device structure (*31*, *39*). Considering the severe electron leakage from PeQWs because of the low LUMO (lowest unoccupied molecular orbital) of CuPc (fig. S25A), further optimization is conducted by increasing the thickness of CuPc and altering HTL from CuPc to 1,1-bis[(di-4-tolylamino)phenyl]cyclohexane (TAPC). As shown in Fig. 3F, the device with thicker CuPc does not show obvious improvement, while the higher LUMO of TAPC substantially enhances the blocking effect for suppressing the electron leakage from PeQWs and enables a higher EQE of 15.2% (measured in ambient air condition without any encapsulation) for green PeQW-based device, which is close to 200 times higher than the previously reported PeLED devices with MIS structure (*37*). A band alignment drawing under forward bias voltage straightforwardly presents the enhanced electron blocking effect (fig. S25). As a high energy barrier between PeQWs and TAPC, electrons are blocked and accumulated into PeQWs, thus higher efficiency for radiative recombination ($\eta_{Radiative}$). It is widely recognized that EQE is directly proportional to $\eta_{Radiative}$, which can be defined by the following formula

$$EQE = \eta_{Injection} \times \eta_{Radiative} \times \eta_{Extraction} \quad (1)$$

Moreover, PAM nanostructure has been widely explored for light coupling by manipulating the refractive index (*40*–*43*). The presence of high light extraction efficiency ($\eta_{Extraction}$), namely, out-coupling efficiency (OCE) has been amply substantiated on nanowires/quantum wires arrays on PAM@Al substrates, with both experimental and simulation results, according to our previous works (*19*, *31*, *33*, *44*–*46*). Meanwhile, the top semitransparent Au electrode can be simply tuned the thickness to modulate the angular-dependent emission profile and microcavity effect in specific device structure to receive the highest OCE (*47*). Therefore, the relatively high EQE in this work can be attributed to the high quality of PeQWs, carrier spatial confinement, and effective light extraction with PAM template, as well as the structural device optimization, revealing their great potential in highly efficient light-emitting applications. Under such consideration, all the devices demonstrated subsequently take TAPC as HTL, unless otherwise specified.

Apart from the promising performance, our PeQW-based Fi-LEDs can also realize light emission in 2D and 3D architectures because Al fiber substrate can be reshaped into diverse profiles with 2D or 3D architectures, benefiting from both of its malleability and plasticity. As shown in Fig. 4A, three Al fibers are sculpted to establish I Love HKUST model and then respectively are fabricated for B-, R-, and G-PeQW–based Fi-LEDs. The photograph shows the EL feature under a constant 8-V bias. It is worth noting that the "HKUST" string is made by patterning one 24-cm-long Al fiber, which is the longest monolithically independent perovskite Fi-LED in the literature, to the best of our knowledge, with a surrounding emission area of nearly 4 cm^2. Here, gallium-indium liquid alloy (hereinafter referred to as "liquid metal") is used as device electrode contacts, and a constant 8-V bias is applied to liquid metal via metal probes to light up three Fi-LEDs at the same time. Similarly, in fig. S26A, the Fi-LED is also fabricated on a filament-shaped Al fiber which is assembled in a lighting bulb and lighted up with a constant 6-V bias. A 3D swirl-shaped substrate is compatible with our PeQW-based Fi-LED fabrication methodology as well, as demonstrated by the EL image at constant 8-V bias in fig. S26B. In addition, by encapsulating our Fi-LEDs with PDMS for resisting moisture and oxygen, as well as stress dispersion, PeQW-based Fi-LED devices with good stretchability, bendability, twistability, and waterproof feature have also been demonstrated. Specifically, as shown in Fig. 4B, a wavy-shaped, which is a widely used architecture for stretchable and wearable electronics (*48*–*51*), is applied to our Fi-LED device to achieve stretchability. A maximum 100% elongation is realized with a constant 6-V bias on the Fi-LED device (Fig. 4C). Also, as shown in Fig. 4D, our Fi-LEDs maintain good EL with a bending radius of 3 mm. Moreover, the wavy architecture device can be even bent with the radius of 2 mm owing to its better tension alleviation (Fig. 4E). It is also very interesting that neither 180° twisting (Fig. 4F) nor water soaking treatment (Fig. 4, G and H) damages the device. Besides the malleability of Al fiber and PDMS protection, such flexible features are also profiting from the 3D PAM template. During deformation, almost all the compressive or tensile stress is concentrated in PAM template, which substantially mitigates the stress and tension on PeQWs (*52*, *53*). Consequently, all the functional materials are sandwiched between three layers of stress reliever: PDMS, PAM, and malleable Al fiber, thus ensuring highly flexible devices. To further evaluate the robustness of Fi-LEDs with PDMS encapsulation, we monitored the EL degradation under various harsh conditions, including bending, stretching, and water soaking. For the bendability test, a 1.5-cm-long Fi-LED device was attached onto different cylinders with different diameters. It can be seen that the EL intensity retains around 80% of its initial value even under a bending radius of 2 mm, as shown in Fig. 4I (black curve). Meanwhile, after 500 bending cycles with a bending radius of 5 mm, the device remains over 85% of its initial EL intensity (red curve in Fig. 4I). For the stretchability test (Fig. 4J), we have found that the device maintains 85% of its initial value even under 100% strain, while it plummets to 50% after 150 stretching cycles under 60% strain, meaning that the mechanical damage from the repeated bending cycles is not negligible. To further improve device mechanical stability, a thinner Fi-LED device with a fiber diameter of 0.2 mm has been fabricated and measured. We have found that the device can retain over 90% EL intensity after 500 bending cycles (star symbol in Fig. 4I) and 80% EL intensity after 150 stretching cycles (star symbol in Fig. 4J). Figure 4K shows the aging test results of the encapsulated device under water soaking. Benefiting from the perfect encapsulation of PDMS, the EL intensity of Fi-LED has no change even after continuous water soaking for more than 1000 hours. The remarkable properties discussed above position the PeQW-based Fi-LED device as one of the highly appealing candidates for flexible and wearable lighting and display applications. Its promising potential for integration onto fabrics further enhances its appeal in this regard.

DISCUSSION

Overall, this work uses fiber-shaped PAM template to uniformly grow PeQWs on Al fibers with 1D, 2D, and 3D architectures. The unique two-step evaporation strategy allows further Fi-LED device fabrication on various unconventional architectures. Ascribed to the malleability and plasticity of Al fiber, in conjunction with the encapsulation and protection with PDMS, the PeQW-based Fi-LEDs have been integrated onto fabric and have rendered bendable, stretchable, twistable, and waterproof devices, which are essential for wearable applications. The facile and unique bonding and fabrication process here allows us to construct arbitrary architectures with multiple colors aiming at future advanced lighting and display applications.

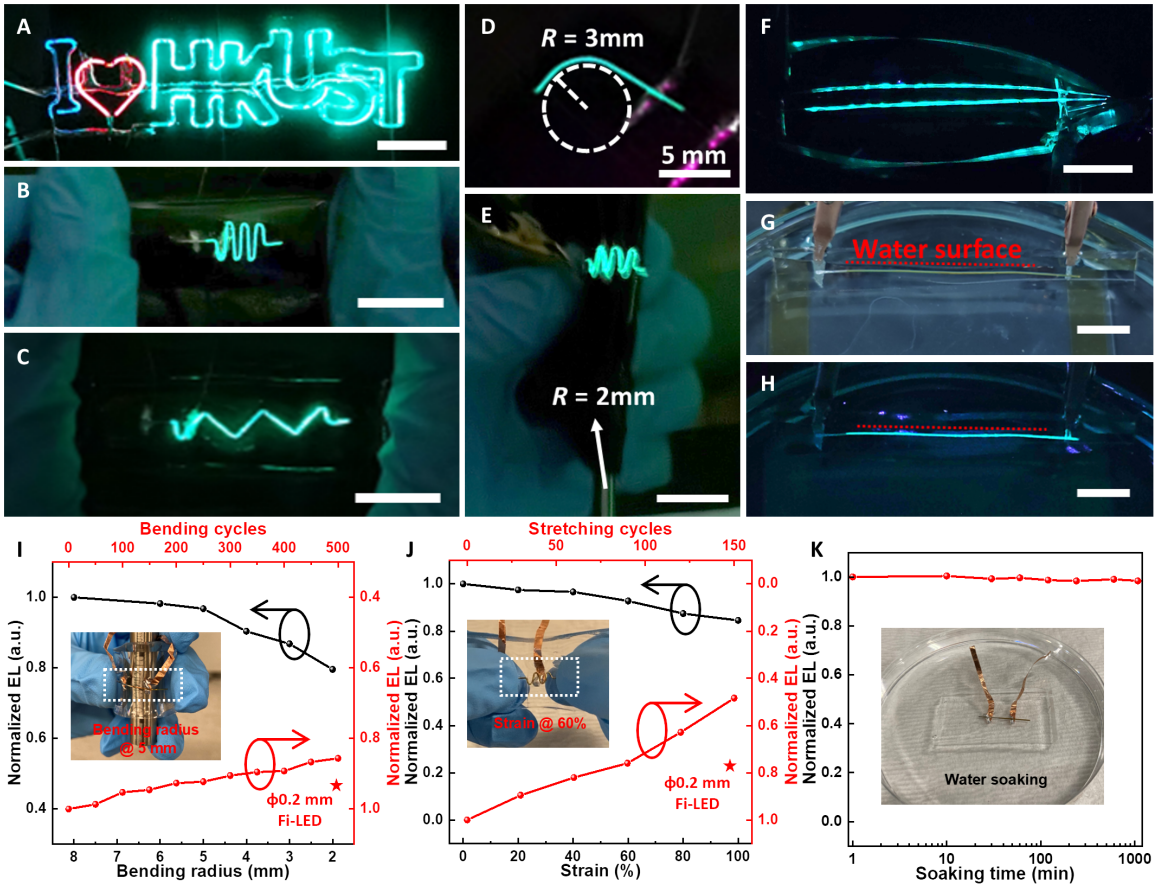

Fig. 4. EL characterizations in diverse scenarios. (**A**) B-, R-, and G-Fi-LEDs with I Love HKUST pattern. (**B** to **C**) Stretchable device with undulant shape before (B) and under (C) stretching. (**D** to **E**) Bendable device respectively with bending radius of 3 mm (D) and 2 mm (E). (**F**) EL images of two Fi-LED devices with 180° twisting. (**G** to **H**) Digital photograph (G) and EL image (H) of an encapsulated device in water. (**I** to **J**) Flexibility evaluations for encapsulated Fi-LEDs: bendability (I) and stretchability (J) characterizations. The insets show the photograph of Fi-LEDs under bending and stretching. (**K**) Aging test of the encapsulated device under continuous water soaking. All the unlabeled scale bars are 1 cm.

MATERIALS AND METHODS

Materials

Unless otherwise stated, all chemicals were purchased from Sigma-Aldrich and used as received without further purification.

MHP precursor preparation

1) G-MHP: CsBr and $PbBr_2$ were dissolved in DMSO with a molar ratio of 1.5:1;

2) B-MHP: CsBr, $PbBr_2$, and $PbCl_2$, were dissolved in DMSO with a molar ratio of 1.5:0.6:0.4;

3) R-MHP: CsBr and PbI_2 were dissolved in DMSO with a molar ratio of 1.2:1. An overnight stirring at 60°C and further filtration by polytetrafluoroethylene 0.45-μm filter were needed for preparing MHP solutions. The concentration of all MHP solutions was 0.1 M, which was defined by the concentration of Pb.

Halide exchange fiber fabrication

Green fiber with $CsPbBr_3$ PeQWs was prepared by the methodology mentioned above, followed by a dip/withdrawal process in CsI and CsCl solutions (both are 16 mg/ml in methanol) for Br-I and Br-Cl exchange, respectively, at a withdrawal speed of 5 cm s^{-1}, thus acquiring G-R and G-B color transition regions on fiber.

Fi-LED fabrication

Al fibers were anodized for PAM template fabrication with the method which can be found in our previous report (*19*). R-, G-, B-MHP solutions were infiltrated in PAM template, at a withdrawal speed of 2 mm s^{-1}, followed by N_2 blowing for removing residual solutions on surface. Then, a 10-min postanneal process was needed to form R-, G-, B-PeQWs, at the temperature of 80°C. Afterward, CuPc and thin Au were successively deposited on PeQWs by a two-step thermal evaporation. Briefly, the as-prepared samples were horizontally fixed on stage for 25-nm CuPc evaporation (~1 Å/s) on the front side then were turned over 180° for another 25-nm CuPc evaporation on another side, to deposit surrounding HTL and cathode, uniformly and continuously. For TAPC devices, TAPC (10 mg/ml; from Ossila) in chlorobenzene was dip-coated on the as-obtained PeQWs at a withdrawal speed of 2 mm s^{-1}. The outward thin Au electrode was deposited by the same evaporation method except the rate (~5 Å/s) and thickness (30 nm). The device active area was defined by the overlapping area between the Al fiber substrate and the Au electrode. Except PAM formation, the whole processes were carried out in N_2-filled glovebox. For PDMS encapsulation, elastomeric PDMS and curing agent (SYLGARD 184 Silicone Elastomer) were mixed at a mass ratio of 20:1 and then degassed in a vacuum oven

for 30 min. The Fi-LEDs were merged into the prepared mixture, and the whole model was cured at room temperature overnight.

Planar device fabrication

PAM substrates were obtained by using Al foils with the same method in fiber -LED fabrication. R-, G-, B-MHP solutions were dropped on PAM substrates, stayed for 2 min for infiltration, and then spin-coated at a rate of 6000 rpm for 1 min to completely remove residual solutions, followed by 10-min annealing at 80°C. Afterward, 25-nm CuPc (~1 Å/s) and 30-nm Au (~5 Å/s) were successively thermally evaporated on PeQWs with shadow masks. The device area was defined by the overlapping area between the Al foil substrate and the Au electrode. For TAPC devices, TAPC was spin-coated on PeQWs at 3000 rpm for 1 min and then crystalized at room temperature for 30 min. Except PAM formation, all the processes were carried out in N_2-filled glovebox.

Measurement and characterization

FIB and SEM were carried out with FEI Helios G4 UX and JEOL 7100F. TEM was operated with JEOL 2010 instrument with 200-kV acceleration voltage, and EDS was achieved by JEOL ARM200F under STEM mode. UV-visible absorption and PL-relevant results were measured respectively by the Varian Cary 500 spectrophotometer and the Edinburgh Instruments FS5 fluorescence spectrometer with an integrating sphere. XRD patterns were gained by using Empyrean (PANanalytical), while XPS/UPS measurements were conducted with Kratos Axis Ultra DLD. TA spectral characterizations were detected by a Helios (Ultrafast Systems) spectrometer, together with a regeneratively amplified Ti:Sapphire laser source (Coherent Legend; 800-nm wavelength, 150-fs pulse, 5 mJ per pulse, and 1-kHz repetition rate). A total of 75% of the 800-nm output pulse was frequency-doubled in a BaB_2O_4 crystal, generating 400-nm pump light. Meanwhile, the remaining portion of the output was concentrated into a sapphire window to produce white light continuum (420 to 780 nm) as probe light. The 400-nm pump beam was focused on the sample with a beam width of about 360 μm and a power intensity of 40 μJ cm^{-2}. LED performance was characterized by a source measurement-unit Keithley 2450 and an Ocean Optics Flame spectrometer with an integrating sphere.

Supplementary Materials

This PDF file includes:

Figs. S1 to S26
Table S1

REFERENCES AND NOTES

1. X. Shi, Y. Zuo, P. Zhai, J. H. Shen, Y. Y. W. Yang, Z. Gao, M. Liao, J. X. Wu, J. W. Wang, X. J. Xu, Q. Tong, B. Zhang, B. J. Wang, X. M. Sun, L. H. Zhang, Q. B. Pei, D. Y. Jin, P. N. Chen, H. S. Peng, Large-area display textiles integrated with functional systems. *Nature* **591**, 240–245 (2021).
2. H. Lee, E. Kim, Y. Lee, H. Kim, J. Lee, M. Kim, H.-J. Yoo, S. Yoo, Toward all-day wearable health monitoring: An ultralow-power, reflective organic pulse oximetry sensing patch. *Sci. Adv.* **4**, eaas9530 (2018).
3. M. Rein, V. D. Favrod, C. Hou, T. Khudiyev, A. Stolyarov, J. Cox, C. C. Chung, C. Chhav, M. Ellis, J. Joannopoulos, Y. Fink, Diode fibres for fabric-based optical communications. *Nature* **560**, 214–218 (2018).
4. C. May, Flexible OLED lighting and signage for automotive application. *The 28th International Workshop on Active-Matrix Flatpanel Displays and Devices (AM-FPD)*, 42–45 (2021).
5. W. Yuan, X. Wu, W. Gu, J. Lin, Z. Cui, Printed stretchable circuit on soft elastic substrate for wearable application. *J. Semicond.* **39**, 015002 (2018).
6. Y. Shi, Z. Zhang, Q. Huang, Y. Lin, Z. Zheng, Wearable sweat biosensors on textiles for health monitoring. *J. Semicond.* **44**, 021601 (2023).
7. C. H. Lee, Y. J. Kim, Y. J. Hong, S. R. Jeon, S. Bae, B. H. Hong, G. C. Yi, Flexible inorganic nanostructure light-emitting diodes fabricated on graphene films. *Adv. Mater.* **23**, 4614–4619 (2011).
8. X. Dai, A. Messanvi, H. Z. Zhang, C. Durand, J. Eymery, C. Bougerol, F. H. Julien, M. Tchernycheva, Flexible light-emitting diodes based on vertical nitride nanowires. *Nano Lett.* **15**, 6958–6964 (2015).
9. F. C. Zhao, D. Chen, S. Chang, H. L. Huang, K. Tong, C. T. Xiao, S. Y. Chou, H. Z. Zhong, Q. B. Pei, Highly flexible organometal halide perovskite quantum dot based light-emitting diodes on a silver nanowire-polymer composite electrode. *J. Mater. Chem. C* **5**, 531–538 (2017).
10. S. Choi, S. Kwon, H. Kim, W. Kim, J. H. Kwon, M. S. Lim, H. S. Lee, K. C. Choi, Highly flexible and efficient fabric-based organic light-emitting devices for clothing-shaped wearable displays. *Sci. Rep. Uk.* **7**, 6424 (2017).
11. S. D. Stranks, H. J. Snaith, Metal-halide perovskites for photovoltaic and light-emitting devices. *Nat. Nanotechnol.* **10**, 391–402 (2015).
12. H. C. Cho, S. H. Jeong, M. H. Park, Y. H. Kim, C. Wolf, C. L. Lee, J. H. Heo, A. Sadhanala, N. Myoung, S. Yoo, S. H. Im, R. H. Friend, T. W. Lee, Overcoming the electroluminescence efficiency limitations of perovskite light-emitting diodes. *Science* **350**, 1222–1225 (2015).
13. G. C. Xing, N. Mathews, S. S. Lim, N. Yantara, X. F. Liu, D. Sabba, M. Gratzel, S. Mhaisalkar, T. C. Sum, Low-temperature solution-processed wavelength-tunable perovskites for lasing. *Nat. Mater.* **13**, 476–480 (2014).
14. Y. Fu, Q. P. Zhang, D. Q. Zhang, Y. Q. Tang, L. Shu, Y. Y. Zhu, Z. Y. Fan, Scalable all-evaporation fabrication of efficient light-emitting diodes with hybrid 2D-3D perovskite nanostructures. *Adv. Funct. Mater.* **30**, 2002913 (2020).
15. Z. K. Tan, R. S. Moghaddam, M. L. Lai, P. Docampo, R. Higler, F. Deschler, M. Price, A. Sadhanala, L. M. Pazos, D. Credgington, F. Hanusch, T. Bein, H. J. Snaith, R. H. Friend, Bright light-emitting diodes based on organometal halide perovskite. *Nat. Nanotechnol.* **9**, 687–692 (2014).
16. K. B. Lin, J. Xing, L. N. Quan, F. P. G. de Arquer, X. W. Gong, J. X. Lu, L. Q. Xie, W. J. Zhao, D. Zhang, C. Z. Yan, W. Q. Li, X. Y. Liu, Y. Lu, J. Kirman, E. H. Sargent, Q. H. Xiong, Z. H. Wei, Perovskite light-emitting diodes with external quantum efficiency exceeding 20 per cent. *Nature* **562**, 245–248 (2018).
17. Y. J. Yoon, J. Y. Kim, A recent advances of blue perovskite light emitting diodes for next generation displays. *J. Semicond.* **42**, 101608 (2021).
18. Q. S. Shan, C. T. Wei, Y. Jiang, J. Z. Song, Y. S. Zou, L. M. Xu, T. Fang, T. T. Wang, Y. H. Dong, J. X. Liu, B. N. Han, F. J. Zhang, J. W. Chen, Y. J. Wang, H. B. Zeng, Perovskite light-emitting/detecting bifunctional fibres for wearable LiFi communication. *Light Sci. Appl.* **9**, 163 (2020).
19. D. Q. Zhang, Q. P. Zhang, B. T. Ren, Y. D. Zhu, M. Abdellah, Y. Fu, B. Cao, C. Wang, L. L. Gu, Y. C. Ding, K. H. Tsui, S. F. Fan, S. Poddar, L. Shu, Y. T. Zhang, D. B. Kuang, J. F. Liao, Y. Lu, K. B. Zheng, Z. B. He, Z. Y. Fan, Large-scale planar and spherical light-emitting diodes based on arrays of perovskite quantum wires. *Nat. Photonics* **16**, 284–290 (2022).
20. B. T. Ren, G. C. O. Yuen, S. B. Deng, L. Jiang, D. J. Zhou, L. L. Gu, P. Xu, M. Zhang, Z. Y. Fan, F. S. Y. Yueng, R. S. Chen, H. S. Kwok, G. J. Li, Multifunctional optoelectronic device based on an asymmetric active layer structure. *Adv. Funct. Mater.* **29**, 1807894 (2019).
21. V. Jamali, F. Niroui, L. W. Taylor, O. S. Dewey, B. A. Koscher, M. Pasquali, A. P. Alivisatos, Perovskite-carbon nanotube light-emitting fibers. *Nano Lett.* **20**, 3178–3184 (2020).
22. W. J. Feng, K. B. Lin, W. Q. Li, X. T. Xiao, J. X. Lu, C. A. Z. Yan, X. Y. Liu, L. Q. Xie, C. B. Tian, D. Wu, K. Wang, Z. H. Wei, Efficient all-inorganic perovskite light-emitting diodes enabled by manipulating the crystal orientation. *J. Mater. Chem. A* **9**, 11064–11072 (2021).
23. Z. X. Wang, M. Elimelech, S. H. Lin, Environmental applications of interfacial materials with special wettability. *Environ. Sci. Technol.* **50**, 2132–2150 (2016).
24. M. N. Zhang, X. H. Wu, A. Riaud, X. L. Wang, F. X. Xie, W. J. Liu, Y. F. Mei, D. W. Zhang, S. J. Ding, Spectrum projection with a bandgap-gradient perovskite cell for colour perception. *Light Sci. Appl.* **9**, 162 (2020).
25. Y. Zhou, X. Qiu, Z. A. Wan, Z. H. Long, S. Poddar, Q. P. Zhang, Y. C. Ding, C. L. J. Chan, D. Q. Zhang, K. M. Zhou, Y. J. Lin, Z. Y. Fan, Halide-exchanged perovskite photodetectors for wearable visible-blind ultraviolet monitoring. *Nano Energy* **100**, 107516 (2022).
26. B. A. Koscher, N. D. Bronstein, J. H. Olshansky, Y. Bekenstein, A. P. Alivisatos, Surface- vs diffusion-limited mechanisms of anion exchange in CsPbBr3 nanocrystal cubes revealed through kinetic studies. *J. Am. Chem. Soc.* **138**, 12065–12068 (2016).
27. J. Y. Yuan, A. Hazarika, Q. Zhao, X. F. Ling, T. Moot, W. L. Ma, J. M. Luther, Metal halide perovskites in quantum dot solar cells: Progress and prospects. *Joule* **4**, 1160–1185 (2020).
28. L. Kang, D. M. Ramo, Z. S. Lin, P. D. Bristowe, J. G. Qin, C. T. Chen, First principles selection and design of mid-IR nonlinear optical halide crystals. *J. Mater. Chem. C* **1**, 7363–7370 (2013).
29. S. Demchyshyn, J. M. Roemer, H. Groiss, H. Heilbrunner, C. Ulbricht, D. Apaydin, A. Bohm, U. Rutt, F. Bertram, G. Hesser, M. C. Scharber, N. S. Sariciftci, B. Nickel, S. Bauer, E. D. Glowacki, M. Kaltenbrunner, Confining metal-halide perovskites in nanoporous thin films. *Sci. Adv.* **3**, e1700738 (2017).
30. D. D. Zhang, Y. Yu, Y. Bekenstein, A. B. Wong, A. P. Alivisatos, P. D. Yang, Ultrathin colloidal cesium lead halide perovskite nanowires. *J. Am. Chem. Soc.* **138**, 13155–13158 (2016).

31. Y. B. Cao, D. Q. Zhang, Q. P. Zhang, X. Qiu, Y. Zhou, S. Poddar, Y. Fu, Y. D. Zhu, J. F. Liao, L. Shu, B. T. Ren, Y. C. Ding, B. Han, Z. B. He, D. B. Kuang, K. F. Wang, H. B. Zeng, Z. Y. Fan, High-efficiency, flexible and large-area red/green/blue all-inorganic metal halide perovskite quantum wires-based light-emitting diodes. *Nat. Commun.* **14**, 4611 (2023).
32. X.-D. Wang, Y.-H. Huang, J.-F. Liao, Z.-F. Wei, W.-G. Li, Y.-F. Xu, H.-Y. Chen, D.-B. Kuang, Surface passivated halide perovskite single-crystal for efficient photoelectrochemical synthesis of dimethoxydihydrofuran. *Nat. Commun.* **12**, 1202 (2021).
33. D. Q. Zhang, L. L. Gu, Q. P. Zhang, Y. J. Lin, D. H. Lien, M. Kam, S. Poddar, E. C. Garnett, A. Javey, Z. Y. Fan, Increasing photoluminescence quantum yield by nanophotonic design of quantum-confined halide perovskite nanowire arrays. *Nano Lett.* **19**, 2850–2857 (2019).
34. L. Cheng, C. Yi, Y. F. Tong, L. Zhu, G. Kusch, X. Y. Wang, X. J. Wang, T. Jiang, H. Zhang, J. Zhang, C. Xue, H. Chen, W. J. Xu, D. W. Liu, R. A. Oliver, R. H. Friend, L. J. Zhang, N. N. Wang, W. Huang, J. P. Wang, Halide homogenization for high-performance blue perovskite electrohiminescence. *Res. Chin.* **2020**, 9017871 (2020).
35. Z. Long, Y. Ding, X. Qiu, Y. Zhou, S. Kumar, Z. Fan, A dual-mode image sensor using an all-inorganic perovskite nanowire array for standard and neuromorphic imaging. *J. Semicond.* **44**, 092604 (2023).
36. J. Fan, H. Yun, X. Zhang, D. Chang, X. Chu, Y. Xie, G. Huang, High-performance pure aluminum coatings on stainless steels by cold spray. *Coatings* **13**, 738 (2023).
37. J. Li, Q. Q. Yu, L. Gan, D. Y. Chen, B. Lu, Z. Z. Ye, H. P. He, Perovskite light-emitting devices with a metal-insulator-semiconductor structure and carrier tunnelling. *J. Mater. Chem. C* **5**, 7715–7719 (2017).
38. F. J. Zhang, J. Z. Song, B. Cai, X. Chen, C. T. Wei, T. Fang, H. B. Zeng, Stabilizing electroluminescence color of blue perovskite LEDs via amine group doping. *Sci. Bull.* **66**, 2189–2198 (2021).
39. W. Bai, T. Xuan, H. Zhao, H. Dong, X. Cheng, L. Wang, R.-J. Xie, Perovskite light-emitting diodes with an external quantum efficiency exceeding 30%. *Adv. Mater.* **35**, e2302283 (2023).
40. B. Hua, Q. F. Lin, Q. P. Zhang, Z. Y. Fan, Efficient photon management with nanostructures for photovoltaics. *Nanoscale* **5**, 6627–6640 (2013).
41. Q. F. Lin, S. F. Leung, L. F. Lu, X. Y. Chen, Z. Chen, H. N. Tang, W. J. Su, D. D. Li, Z. Y. Fan, Inverted nanocone-based thin film photovoltaics with omnidirectionally enhanced performance. *ACS Nano* **8**, 6484–6490 (2014).
42. S. F. Leung, L. L. Gu, Q. P. Zhang, K. H. Tsui, J. M. Shieh, C. H. Shen, T. H. Hsiao, C. H. Hsu, L. F. Lu, D. D. Li, Q. F. Lin, Z. Y. Fan, Roll-to-roll fabrication of large scale and regular arrays of three-dimensional nanospikes for high efficiency and flexible photovoltaics. *Sci. Rep. Uk.* **4**, 4243 (2014).
43. R. Yu, K. L. Ching, Q. F. Lin, S. F. Leung, D. Arcrossito, Z. Y. Fan, Strong light absorption of self-organized 3-D nanospike arrays for photovoltaic applications. *ACS Nano* **5**, 9291–9298 (2011).
44. Q. Zhang, M. M. Tavakoli, L. Gu, D. Zhang, L. Tang, Y. Gao, J. Guo, Y. Lin, S.-F. Leung, S. Poddar, Y. Fu, Z. Fan, Efficient metal halide perovskite light-emitting diodes with significantly improved light extraction on nanophotonic substrates. *Nat. Commun.* **10**, 727 (2019).
45. Q. P. Zhang, D. Q. Zhang, L. L. Gu, K. H. Tsui, S. Poddar, Y. Fu, L. Shu, Z. Y. Fan, Three-dimensional perovskite nanophotonic wire array-based light-emitting diodes with significantly improved efficiency and stability. *ACS Nano* **14**, 1577–1585 (2020).
46. Q. Zhang, D. Zhang, Y. Fu, S. Poddar, L. Shu, X. Mo, Z. Fan, Light out-coupling management in perovskite LEDs—What can we learn from the past? *Adv. Funct. Mater.* **30**, 2002570 (2020).
47. Y. F. Miao, L. Cheng, W. Zou, L. H. Gu, J. Zhang, Q. Guo, Q. M. Peng, M. M. Xu, Y. R. He, S. T. Zhang, Y. Cao, R. Z. Li, N. N. Wang, W. Huang, J. P. Wang, Microcavity top-emission perovskite light-emitting diodes. *Light Sci. Appl.* **9**, 89 (2020).
48. C. Y. Liu, N. G. Huang, F. Xu, J. D. Tong, Z. W. Chen, X. C. Gui, Y. L. Fu, C. S. Lao, 3D printing technologies for flexible tactile sensors toward wearable electronics and electronic skin. *Polymers* **10**, 629 (2018).
49. W. Wu, Stretchable electronics: Functional materials, fabrication strategies and applications. *Sci. Technol. Adv. Mat.* **20**, 187–224 (2019).
50. H. Oh, J. Y. Oh, C. W. Park, J. E. Pi, J. H. Yang, C. S. Hwang, High density integration of stretchable inorganic thin film transistors with excellent performance and reliability. *Nat. Commun.* **13**, 4963 (2022).
51. Z. Xue, T. Dong, Z. Zhu, Y. Zhao, Y. Sun, L. Yu, Engineering in-plane silicon nanowire springs for highly stretchable electronics. *J. Semicond.* **39**, 011001 (2018).
52. Y. Y. Zhu, L. Shu, S. Poddar, Q. P. Zhang, Z. S. Chen, Y. C. Ding, Z. H. Long, S. M. Ma, B. T. Ren, X. Qiu, Z. Y. Fan, Three-dimensional nanopillar arrays-based efficient and flexible perovskite solar cells with enhanced stability. *Nano Lett.* **22**, 9586–9595 (2022).
53. Y. Zhu, Q. Zhang, L. Shu, D. Zhang, Z. Fan, Recent progress of efficient flexible solar cells based on nanostructures. *J. Semicond.* **42**, 101604 (2021).

Acknowledgments: We acknowledge the support from the Material Characterization and Preparation Facility (MCPF) and the State Key Laboratory of Advanced Displays and Optoelectronics Technologies at HKUST. We acknowledge the assistance of Southern University of Science and Technology Core Research Facilities. Z.F. acknowledges the support from the New Cornerstone Science Foundation through the XPLORER PRIZE and Hong Kong Alliance of Technology and Innovation through BOCHK Science and Technology Innovation Prize. **Funding:** This work was supported by Hong Kong Research Grant Council (N_HKUST657/22, 16205321, 16309018, and 16214619), Shen Zhen Science and Technology Innovation Commission (JCYJ20170818114107730 and JCYJ20180306174923335), Innovation Technology Fund (GHP/014/19SZ), Guangdong-Hong Kong-Macao Intelligent Micro-Nano Optoelectronic Technology Joint Laboratory (2020B1212030010), and Foshan Innovative and Entrepreneurial Research Team Program (2018IT100031). **Author contributions:** Conceptualization: Z.F. and B.R. Methodology: B.R., D.Z., and Q.Z. Device fabrication: B.R., D.Z., Y.D., Q.Z., S.P., C.L.J.C., B.C., C.W., and Y.Z. Characterizations: B.R., D.Z., X.Q., Y.F., J.-F.L., and D.-B.K. Supervision: Z.F. Writing—original draft: B.R. Writing—review and editing: B.R., D.Z., H.Z., and Z.F. **Competing interests:** The authors declare that they have no competing interests. **Data and materials availability:** All data needed to evaluate the conclusions in the paper are present in the paper and/or the Supplementary Materials.

Submitted 23 November 2023
Accepted 11 April 2024
Published 15 May 2024
10.1126/sciadv.adn1095